AI-based autism identification from hyperspectral imaging detection of oxidative stress in pediatric red blood cells

Roupen Vartian[1,§], Anna Sansone[1,§], Gessica Batani[1], Marina Marini[2], Enzo Grossi[3], Antonia Parmeggiani[2,4], Vincenzo Davide Catania[5], Mario Lima[5], Alessandro Ghezzo[6], Cristina Panisi[7], Marida Angotti[4], Provvidenza M. Abruzzo[2], Carmela Serpe[2], Arianna Vignini[8], Ellas Spyratou[9], Efstathios P. Efstathoupoulos[9], Chryssostomos Chatgilialoglu[1,10], Carla Ferreri[1,11]*

[§]First co-authors
*Corresponding author: Carla Ferreri; email: carla.ferreri@cnr.it

SUPPLEMENTARY INFORMATION

Supplementary Notes

1. HSI-based RBC membrane analysis

Hyperspectral Imaging (HSI) technology relies on the "hypercubes", i.e. three-dimensional datasets which are stored for every pixel and contain the two-dimensional (x,y) spatial information collected by EDFM, as well as the localized scattering spectral information pixel-by-pixel collected by the hyperspectral imaging setup.[1-3] In other words, HSI has greatly advanced the use of typical RGB images, as each pixel now encodes information across a broad range of wavelengths (typically in the VNIR region, 400–1000 nm). Supplementary Fig. 1a illustrates a standard HDFM configuration, in which the specimen under study (in our case, red blood cells) is illuminated with white light. In Fig. S1b, a region of interest (ROI) is visible on an RBC specimen, where images are collected at multiple λ values. Thus, for each (x, y) point on the resulting image, a value of spectral intensity (I) is stored for each λ, providing the spectral fingerprint for each point. The spectral library and corresponding bands are displayed in Supplementary Figure 1c and d.

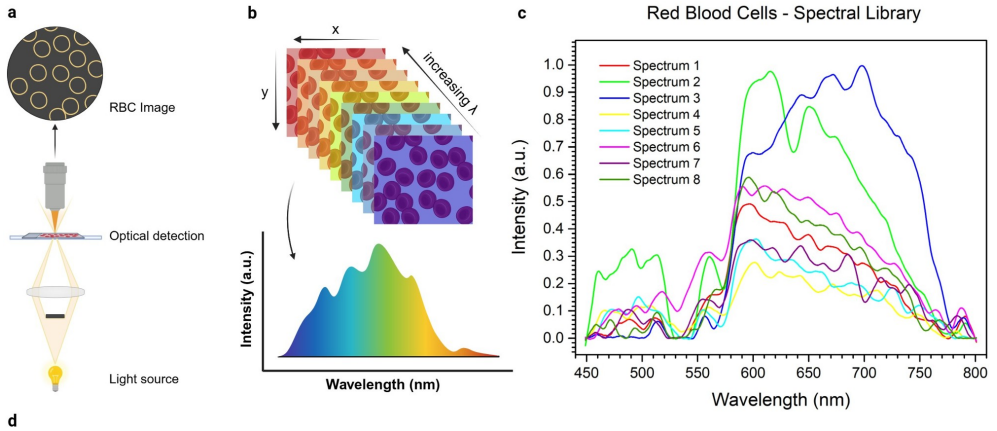

d

	Spectral library bands									
	450-500	**500-525**	**525-550**	**550-575**	**575-600**	**600-625**	**625-650**	**650-675**	**675-700**	**700-800**
Spectrum 1	488 (s)	511 (s)		563	595 (s)		626, 649 (s)	670	699	790 (s)
Spectrum 2	460 (s), 490 (s)	512 (s)		561 (s)		604, 615 (s)		651 (s), 674		718, 753, 791 (s)
Spectrum 3		514 (s)		557 (s)	599 (s)		643 (s)	668 (s)	698 (s)	789 (s)
Spectrum 4	467	507		559 (s)		601 (s), 624	643	670 (s)	692	709 (s), 748 (s), 783 (s)
Spectrum 5	472, 497 (s)	516		555 (s)	595	602 (s)	629	657 (s)	693 (s)	726 (s), 749 (s)
Spectrum 6	477 (s), 495 (s)	518 (s)		558 (s)	590 (s)	610 (s)	627 (s), 649 (s)	674 (s)	694 (s)	727, 764 (s), 787 (s)
Spectrum 7	487 (s)	508 (s)		557 (s)	597 (s)	617 (s)	643 (s)	663 (s)	685 (s)	715 (s), 727, 740 (s), 762, 784 (s)
Spectrum 8	458 (s), 471 (s), 493 (s)	513 (s)	547	566	595 (s)	618 (s)	636, 649	663	679, 696 (s)	719, 768 (s)

e

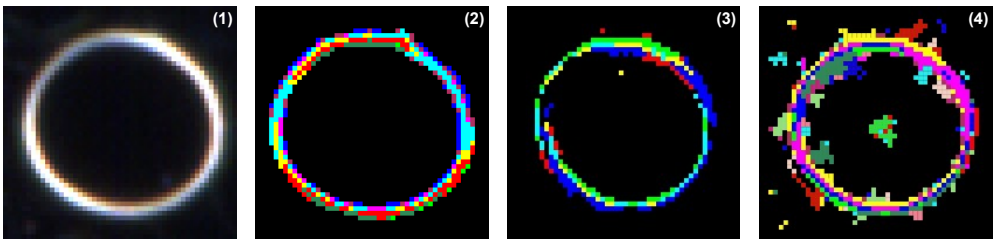

Supplementary Figure 1 – **The HSI set-up**: a) the typical dark field microscopy detection; b) the hyperspectral cube collects image data of (x,y) and λ-I (I for intensity) values at multiple wavelengths along with the (x,y) values for each

pixel; c) the HSI spectral library of RBC, made of eight end members in the 450-800 nm range; d) the list of the eight spectral endmembers (spectrum numbers are arbitrary) with their main bands (s, strong); e) the optical image of RBC (1) is shown with the HSI-mapping using the eight endmembers (2), less endmembers with under mapping effect (3) and more endmembers with overmapping effect (4). Panels a) and b) were created by the Authors.

Usually, a hyperspectral dark-field imaging setup requires a scanning stage, a spectrometer, and a sensitive CCD camera. Initially, optical dark-field imaging is performed, where an optimal region of interest on the sample is identified. Hyperspectral images were acquired using “push broom” (also known as “line scan”) technique in which the glass slide supporting the blood sample on the motorized stage of microscope was moved across the field of view of the microscope during image acquisition.
The spectral features for each pixel are stored using a VIS-NIR spectrometer connected to a CCD camera, yielding a hypercube for each (x, y).[4,5] Under the illumination of a white light source, without the need for additional labels, the HDFM configuration collects the elastically scattered light from the specimen. It blocks directly transmitted light, thereby achieving a higher signal-to-noise ratio (SNR) than a typical optical system and increasing sensitivity. A standard DFM output image depicts a noiseless dark background with clearly distinct boundary-bright appearing objects, where information on the sample’s size, composition, morphology, and location can be extracted.[8,9]
The resulting image is severely affected not only by the intrinsic features of the studied material but also by the other various exogenous factors like the medium, illumination setup, light’s angle of incidence, and the objective’s numerical aperture. To mitigate these problems, CytoViva™ created the enhanced dark-field (EDF) illuminator (CytoViva, Auburn, Al, USA), commonly used in medical and biological applications, which manages to efficiently utilize each one of these features and increase SNR up to ten times by fixing lightpath’s geometry (light is guided and gets collimated directly into the condenser).[10,11] By combining high numerical aperture (NA) oil-immersion objectives, the scattered light can be captured at wider angles, thus resolving biological nanoparticles (even of 20-200 nm size).[12] The calibration of the measurements is performed using two commercially available standard references (NIST polystyrene standard and the White reference standard).
As soon as the hypercubes have been stored for each pixel (images collected for our study contain 696 x 696 pixels) of the RBC image, Environment for Visualizing Images (ENVI, Exelis Visual Information Solutions) software version 4.4, is used visualizes images from three red blood cells selected as regions of interest (ROIs), with such selection repeated three times per each blood sample (n=9 blood samples). To display the data on a PC screen, a specialized algorithm transforms each hypercube into a standard RGB composite. This process is used solely for visualization and does not fundamentally alter the underlying hyperspectral features. Following image acquisition, mean spectral signatures were extracted from the nine ROIs by calculating average scattering values across the 400–1000 nm range. When we mention ENVI, it includes the performance of analyses such as: PCA analysis and MNF (Minimum Noise Fraction), which simplify the data, without losing important “features”, and the "small noise" that the Referee mentions is likely partitioned into the later MNF bands and discarded, leaving only the "true" spectral differences for SAM to act upon. ENVI also includes Spectral Feature Fitting (SFF), which compares the depth and shape of specific absorption pits in the graph.
ENVI analyzes the acquired hyperspectral images and generates spectral graphs. By a careful manual process, the spectral graphs are optimized leading to the RBC spectral library of 8 spectral endmembers, from the initial 15 endmembers identified by the system. These hyperspectral graphs are then used as endmembers for subsequent classification via the Spectral Angle Mapper (SAM) algorithm.[6,7]
The eight spectral endmembers (Supplementary Fig. 1c, with bands in the Table of Supplementary Figure 1d) were found to cover the optical image whereas, using fewer or more endmembers, under- or over-overmapping effects were detected (Supplementary Figure 1e).

2. Spectral Angle Mapper (SAM) classification algorithm

The SAM algorithm superimposes reflectance spectra as vectors in an n-dimensional space, where n is the number of spectral bands per spectrum. It classifies each pixel using a threshold angle between each pixel vector and the spectral endmember. The smaller the angle between a pixel and an end member, the closer the match between them. The radian was set up at 0.1. By assigning a color code to the spectral endmembers identified in the sample, the optical image is converted into a false-colored spectral image, utilizing many color channels (8 different colors corresponding to the 8 different spectral endmembers), and the satisfactory match between optical and spectral data can be visualized. In case a pixel is unable to match at an angle smaller than the threshold with any of the end members, it is considered unclassified, and the pixel is colored black. THE MAPPPING RESULTS IN THE DISTRIBUTIONS OF THE EIGHT HYPERSPECTRAL GRAPHS OF THE RBC.

When RBC images from other OS experiments and from the children cohort undergo the HSI protocol, the distributions of the eight endmembers of the spectral library are registered and these data are then processed statistically (comparison with the healthy RBC endmembers distributions and evaluation of the significant changes, see Tables Figures 1 and 3) as well as by AI.

Supplementary Methods

1. **Image detection procedure**

Details of Fig. 1 in the Main text and more information of the Experimental methodology are given here.

a. **Procedure to eliminate lamp spectrum background**

In the present study, the spectral library was constructed using a different procedure compared to previously reported studies.[13,14] In particular, the acquisition intensity increased from ~500 a.u. to ~5000 a.u. (arbitrary unit). We also eliminated the effects of the light source and the light guide on the collected HSIs and, consequently, on the class distribution data, which form the basis of our study. In Supplementary Fig. 2, the procedure is detailed, with the first spectral endmember (spectrum 1) used as an example.

In Supplementary Fig. 2a, the first spectral endmember is shown exactly as the instrument captures it, whereas in Supplementary Fig. 2b, the lamp spectrum is displayed. The procedure, whose result is shown in Supplementary Fig. 2c, properly removes the lamp spectrum, thus normalizing a parameter crucial for ENVI accuracy.

Initially, the recorded lamp spectrum's intensity reached ~3000 a.u. By removing the lamp spectrum, the intensity level decreases, and significant noise appears in both the low and high wavelength areas (<450 nm and >800 nm). For this reason, these areas are being cut (subsetted), as shown in Supplementary Fig. 2d. The spectrum is thus finally focused in the range between 450 and 800 nm. Supplementary Fig. 2e shows the final spectrum 1 shape after baseline correction using the Statistics-sensitive Non-linear Iterative Peak-clipping (SNIP) algorithm (100 iterations) to remove luminescence. Additionally, the Savitzky-Golay filter was applied to smooth the data. In Supplementary Fig. 2f, from left to right, the original spectra of the full spectral library are given, the same spectra after the lamp light impact have been eliminated, and the range is subsetted to 450-800nm, and lastly, after SNIP algorithm has been used for luminescence elimination and baseline correction of the eight spectra. The Baseline correction on the spectral library was used only for the indication of the spectral bands of each endmember and the evaluation of the qualitative characteristics of the spectral library. It is not necessary to apply the mapping procedure to the collected HSIs. For each collected HSI, lamp spectrum removal and spectral subsetting were applied, but no baseline correction was performed.

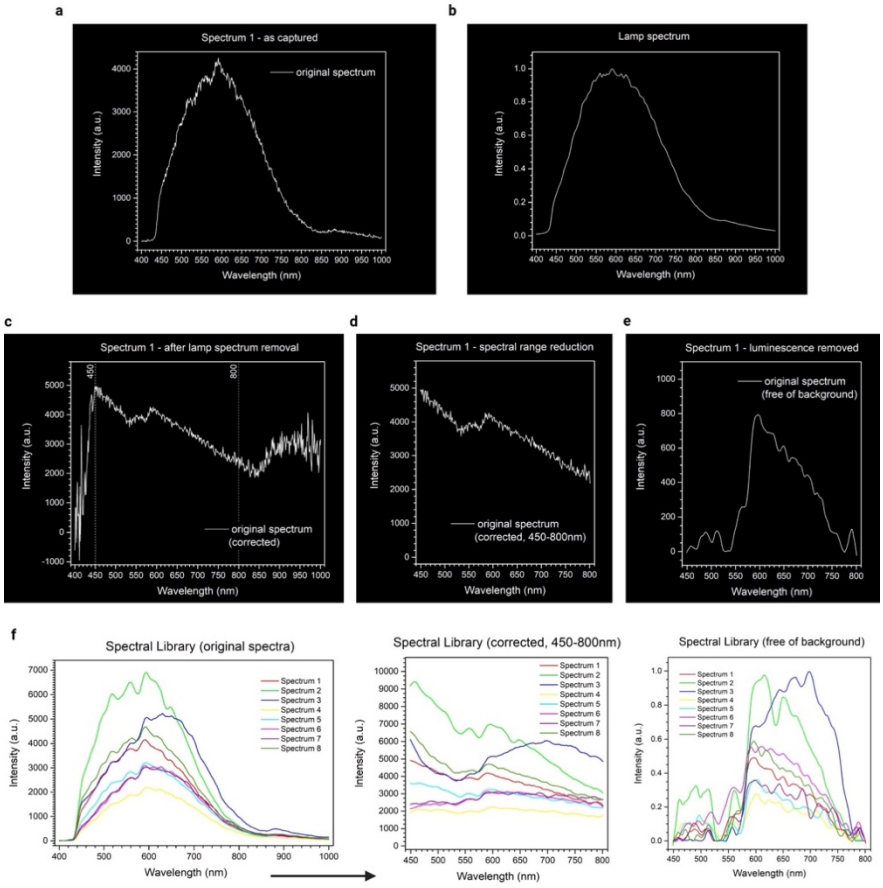

Supplementary Figure 2. Analytical guide for the treatment of the collected spectra to eliminate lamp spectrum and remove luminescence a) Spectrum 1 of the spectral library as captured by the instrument; b) The lamp spectrum of the used setup; c) The spectrum (a), after the lamp spectrum has been removed. A significant noise can be seen to be created in the ranges of 400-450nm and 800-1000nm; d) The spectrum (c), after noisy areas have been removed. Our study focuses on the range between 450-800nm (VIS-NIR); e) The spectrum (d), after baseline correction has been applied using SNIP algorithm to remove luminescence, and data smoothing using Savitzky-Golay filter (2nd order, 11 points), and is offset for clarity; f) From left to right, the original spectra of the spectral library that were recorded by the instrument, the same spectral library after lamp spectrum removal and spectral subsetting, and finally, the eight spectra after luminescence removal. On all of these three graphs, Savitzky-Golay filtering method has also been applied for data smoothing.

With these corrections to the previously reported methodology, the previously reported[13,14] and the actual spectral libraries of the RBC are shown in Supplementary Fig. 3.

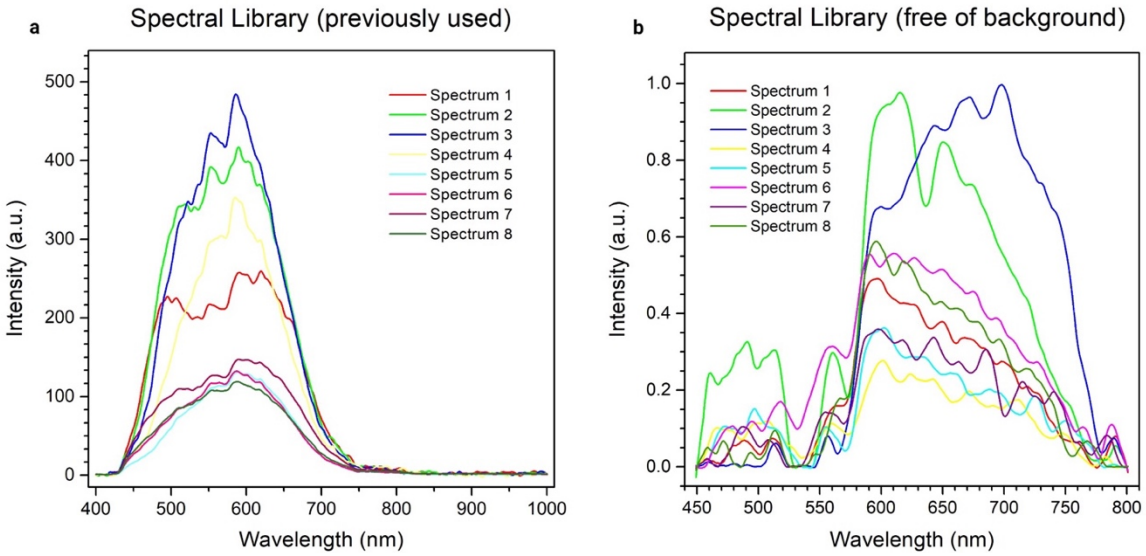

Supplementary Figure 3. Hyperspectral imaging (HSI) of RBC. Comparison with the previous (left) and actual (right) HSI spectral graphs referred to RBC membrane using hyperspectral dark field microscopy (HDFM), after eliminating the lamp spectrum and luminescence background.

b. HSI analysis of RBC molecular components and spectral information for the interpretation of RBC spectral endmembers.

Human hemoglobin, cholesterol, 7-ketocholesterol, spectrin from human erythrocytes, phosphate buffer 10mM (PBS pH 7.4), C18 (plasm) 20:4-PC (1-(1Z-octadecenyl)-2-arachidonoyl-sn-glycero-3-phosphocholine) were purchased from Merck (Darmstadt, Germany); egg lecithin was a gift from Lipoid GmbH (Ludwigshafen, Germany).
These molecular components were used as representatives of the RBC membrane and sub-membrane compartments, and the HSI analysis was performed on solutions or suspensions at a molarity similar to that found in biological systems, prepared as follows:

- suspension of 10mM cholesterol in 10 mM phosphate buffer saline PBS (pH 7.4): 0.77 mg of cholesterol (0.002 mmol) was suspended in 0.2 mL of PBS;
- suspension of 10mM 7-ketocholesterol in 10 mM PBS (pH 7.4): 0.8 mg of 7-ketocholesterol (0.002 mmol) was suspended in 0.2 mL of PBS;
- solution of 1.1 mM human hemoglobin in 10 mM PBS (pH 7.4): 75 mg of human hemoglobin (0.0011 mmol) was dissolved in 1 mL of PBS;
- suspension of 0.2 mM human oxidized hemoglobin by 30% H_2O_2: 15 mg of human hemoglobin (0.0002 mmol) were suspended in 1 mL of 30% H_2O_2 (1h oxidation at room temperature). Oxidized human hemoglobin was prepared by treatment of hemoglobin at three different H_2O_2 concentrations (1.5%, 3% and 30%).[15] The best image was obtained for the product at 30% H_2O_2 concentration (30%).
- 130 mM egg lecithin phospholipids as a multilamellar liposome suspension in 10 mM PBS (pH 7.4) prepared as described in the literature.[13] 100 mg of egg lecithin film was suspended in 1 mL of PBS; It is also important to mention that liposome samples were subjected to centrifugation and subsequent PBS washing to remove all excess background interference.
- Solution of 0.41 µM Spectrin in 10 mM PBS (pH 7.4): 40 mg of spectrin (0.000082 mmol) was dissolved in 0.2 mL of PBS (pH 7.4)

The samples for HSI acquisition were prepared by depositing approximately 5 µL of the PBS suspension or solution containing cholesterol, cholesterol oxide, haemoglobin, oxidised haemoglobin, spectrin, on a glass slide; 10 µL of the suspension was used for liposomes.

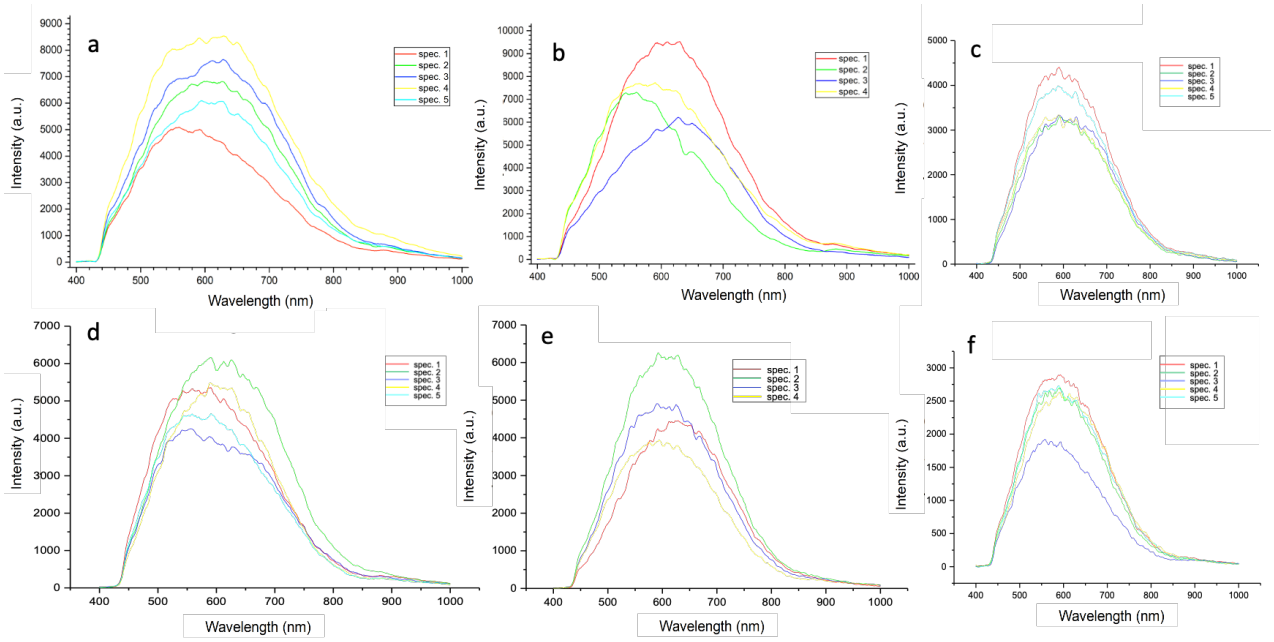

Supplementary Figure 4. Spectral libraries of the six pure components used to acquire HSI data: a) cholesterol; b) cholesterol oxide (7-keto cholesterol); c) egg lecithin liposomes; e) hemoglobin; f) oxidized hemoglobin; f) spectrin. In all spectra, the lamp background spectrum was eliminated. Typical spectral bands of each component were identified from the spectral vs. intensities lists and reported in the Supplementary Table 1A.

Supplementary Table 1. A) HSI analysis of representative RBC molecular components of the RBC membrane and sub-membrane compartments, with their spectral endmembers (spectrum numbers are arbitrary) and leading bands (s, strong). Superscripts indicating the presence in the RBC spectral library: a) Component of the spectral endmember 1; b) Component of the spectral endmember 2; c) Component of the spectral endmember 3; d) Component of the spectral endmember 4; e) Component of the spectral endmember 5; f) Component of the spectral endmember 6; g) Component of the spectral endmember 7; h) Component of the spectral endmember 8. B) Details of the identification of the spectral bands reported in A) in the HSI spectral library of RBC (region 450-800nm - VIS-NIR).

		450-500	500-525	525-550	550-575	575-600	600-625	625-650	650-675	675-700	700-800
Cholesterol	**Spectrum 1**	472 [e,h], 497 [e]	522	547	558(s) [c,f,g]	591 (s)	608	627, 649(s) [a, f]	673		728 [f,g]
	Spectrum 2	474 [f, 497]				579 (s)	601(s) [a,b,c,d,e]	627(s) [a, f], 647(s)	666	698[c]	
	Spectrum 3	497[e]	521	549 (s)		596	611(s)	628(s)	669 [c]	694(s) [c,d,f,h]	785 [c,d,f,g]
	Spectrum 4	473, 498	522	548	571	590 (s) [f]	611	629(s) [d,e], 649(s) [a,f,h]	671 [d]	694	745 [d], 779 [d]
	Spectrum 5	494	520	543	564	594 (s)	610(s) [f]	626 (s) [a]	651 (s) [b], 672	693[e]	775

		450-500	500-525	525-550	550-575	575-600	600-625	625-650	650-675	675-700	700-800
Cholesteryl oxide	**Spectrum 1**	497 [e]				591 (s)	610 (s) [f]	628 (s), 649 (s) [a]			
	Spectrum 2	496	520	541 (s)	559 (s) [d]	585	622 (s) [d]	647 (s)		694	
	Spectrum 3	498	520		553	592 (s)		627 (s) [f], 648 (s)			
	Spectrum 4	474, 498	521	544	562	589 (s)		623 (s), 646 (s) [c, d, g]			780

		450-500	500-525	525-550	550-575	575-600	600-625	625-650	650-675	675-700	700-800
Spectrin	**Spectrum 1**				557 [g]	590 (s)		627(s) [a,f], 647(s) [a]			
	Spectrum 2			543	563 (s) [a], 573	590 (s)	610 (s) [f]	627			
	Spectrum 3	494			554(s) [e], 575 (s)	590 (s)	611		651[b]		
	Spectrum 4				559(s) [d]	588 (s)	608, 615(s) [b,g,h]	628	653, 672	696	
	Spectrum 5		518 [f]	546		590 (s) [f]	613	627		697	

		450-500	500-525	525-550	550-575	575-600	600-625	625-650	650-675	675-700	700-800
Egg lecithin	**Spectrum 1**	496	519		555	590 (s)	610 (s) [f]	628	668	696	723
	Spectrum 2	493 [h]	520	541	559, 574	592		629(s) [e]	653(s) [e]		726 [e,f,g], 746 [e]
	Spectrum 3	491[a,b,g]	521		562	591 (s)	612	627 (s) [f]	651(s) [b]	693	
	Spectrum 4	496	520		559(s) [d], 575	587 (s)	611 (s)	632(s) [h], 648(s)	662		
	Spectrum 5	498	519	543 (s) [h]		590 (s) [f]		627(s), 644	664	694 [e]	

		450-500	500-525	525-550	550-575	575-600	600-625	625-650	650-675	675-700	700-800
Hemoglobin	**Spectrum 1**	495[f]		527	561	588 (s)	614		651	695	
	Spectrum 2		522			588 (s)	611 (s)	628 (s), 649	672	695	
	Spectrum 3	497 [e]	518 [f]			589 (s)	608 (s)	629(s) [e]	652		
	Spectrum 4	495 [f]	518 [f]			592 (s)		625	650(s)	682(s) [g,h]	
	Spectrum 5	498	519			592		629, 649			

		450-500	500-525	525-550	550-575	575-600	600-625	625-650	650-675	675-700	700-800
Hemoglobin oxide	**Spectrum 1**	495 [f]	517 [c,d,h]	542		594 (s)		648	669	697	
	Spectrum 2	497 [e]	519			595 (s) [a,e,g,h]		626 (s), 648		698	
	Spectrum 3	494	519	540	559	590 (s) [f]	608	626 (s) [a], 649 (s) [a,f,h]	671(s) [a,b,d,f]	695	
	Spectrum 4	496			572	592 (s)	610 (s) [f]	629(s) [a,e], 648			719 [b,g,h]

B

	450-500	500-525	525-550	550-575	575-600	600-625	625-650	650-675	675-700	700-800
Spectrum 1	488	511		563	595		626, 649	670	699	790
	Egg (491)	-		Spectrin (563)	Hem. ox. (595)		Spectrin/Chol./ Chol. ox./ Hem ox. (626, 649)	Hem. ox. (671)		-
Spectrum 2	460, 490	512		561		604, 615		651, 674		718, 753, 791
	Egg (491)	-				Chol. (601), Spectrin (615)		Egg/Chol. (651) Hem. ox. (671)		Hem. ox. (719)
Spectrum 3		514		557	599		643	668	698	789
		Hem. ox. (517)		Chol. (558)	Chol (601)		Chol. ox. (646)	Chol. (669)	Chol (694)	Chol (785)
Spectrum 4	467	507		559		601, 624	643	670	692	709, 748, 783
	-	-		Chol. ox./ /Egg (559)		Chol (601), Chol. ox. (622)	Chol. ox. (646)	Hem. ox./ Chol/ (671)	Chol (694)	Chol (745, 785)
Spectrum 5	472, 497	516		555	595	602	629	657	693	726, 749
	Chol (472), Chol/Chol. ox./ Hem/Hem. ox. (497)	Hem. ox. (517)		Spectrin (554)	Hem ox (595)	Chol (601)	Chol/Egg/Hem/Hem . ox. (629)	Egg (653)	Chol (694)	Egg (726, 746)
Spectrum 6	477, 495	518		558	590	610	627, 649	674	694	727, 764, 787
	Chol (474), Hem/Hem ox (495)	Hem/Spectrin (518)		Chol (558)	Chol/Spectrin/Egg /Hem ox (590)	Chol/Chol. ox./ Egg/Spectrin/Hem ox (610)	Chol/Chol. ox./ Egg/Spectrin/ (627) Chol/Hem ox (649)	Hem. ox. (671)	Chol (694)	Chol (728)/ Egg (726), Chol (785)
Spectrum 7	487	508		557	597	617	643	663	685	715, 727, 740, 762, 784
	Egg (491)	-		Spectrin,Chol (558)	Hem ox (595)	Spectrin (615)	Chol. ox. (646)	-	Hem (682)	Hem ox (719) Chol (728)/Egg (726), Chol (785)
Spectrum 8	458, 471, 493	513	547	566	595	618	636, 649	663	679, 696	719, 768
	Chol (472), Egg (493)	Hem. ox. (517)	Egg (543)		Hem ox (595)	Spectrin (615)	Egg (632), Chol/Hem ox (649)	-	Hem (682) Chol (694)	Hem ox (719)

2. RBC membrane isolation from whole blood samples and fatty acid-based membrane lipidomic analysis

The EDTA-treated whole blood samples, both in the blood oxidation experiment and in the study of NT and ASD subjects, were worked up according to the previously described procedure.[14]
Supplementary Table 2 shows the HSI spectral distributions percentages of the 0.75% H_2O_2-treated RBC sample in comparison with the control RBC signature, and Supplementary Table 3 shows the fatty acid composition of the RBC membranes of the same samples. Data are given as mean ± s.e.m. (standard error of the mean). The fatty acid values are given in % relative quantitative units (% rel. quant.) which means that: i) the quantification of each fatty acid was done by identification and calibration with the appropriate standard reference; ii) the sum of the whole recognized fatty acid quantities constitutes 100% where each fatty acid is expressed as a percent of the whole quantity.

Supplementary Table 2. HSI data of the RBC oxidative model. Spectral distributions of the eight endmembers in the 0.75% H_2O_2-treated RBC in comparison with the control RBC signatures. Three different blood samples are used, following the RBC image acquisition described in the Method. The total number of RBC images analysed in this experiment is 27. Statistical comparisons were performed by applying an unpaired two-sided t-test.

	0.75% H_2O_2 experiment			
	Untreated n = 3	Treated n = 3	Delta (%)	P - value
	Mean ± SEM	Mean ± SEM		
Spectrum 1	17.16 ± 0.26	17.47 ± 0.35	+ 0.31	-
Spectrum 2	11.34 ± 1.34	11.52 ± 0.44	+ 0.18	-
Spectrum 3	6.25 ± 0.31	5.47 ± 0.05	- 0.78	-
Spectrum 4	16.29 ± 0.61	16.81 ± 0.29	+ 0.52	-
Spectrum 5	27.14 ± 1.01	27.21 ± 0.21	+ 0.08	-
Spectrum 6	1.32 ± 0.48	2.36 ± 0.26	+ 1.04	-
Spectrum 7	16.10 ± 0.55	15.47 ±0.34	- 0.63	-
Spectrum 8	4.41 ± 0.45	3.68 ± 0.32	- 0.72	-

Supplementary Table 3. Fatty acid composition of RBC membranes. Results of the RBC membrane lipidome composition in fatty acids (mean values ± standard error of the mean, SEM) isolated from untreated and 1.5% H_2O_2-treated EDTA-containing whole blood samples as described in the Main text. Fatty acid methyl esters (FAME) are expressed as relative percentages (mean values ± standard error of the mean, SEM) of the quantitative values of each fatty acid obtained by calibration curves of the standards (% rel.quant.); Unsaturation index (UI) = [(TOT MUFA * 1) + (C18:2*2) + (C20:3 *3) + (C20:4*4) + (C20:5 *5) + (C22:6 *6)]; Peroxidation index (PI) = [(TOT MUFA* 0,025) + (C18:2*1) + (C20:3 *2) + (C20:4*4) + (C20:5 *6) + (C22:6 *8)]. Statistical comparisons were performed by applying an unpaired two-sided t-test ; the exact p-values are shown in the table.

FAME and Indexes	Untreated RBC (n=9) % rel. quant. mean ± SEM	1.5% H_2O_2-treated RBC (n=9) % rel. quant. mean ± SEM	p-values
C16:0	33.51±1.21	39.25±1.58*	0.010
6cis C16:1	0.24±0.02	0.27±0.03	0.41
9cis C16:1	0.23±0.02	0.23±0.04	>0.9
C18:0	22.41±1.93	26.34±1.09	0.09
9cis C18:1	13.76±0.85	12.06±0.71	0.144
11cis C18:1	1.08±0.07	0.74±0.14*	0.045
C18:2 omega 6	8.71±0.83	7.30±0.35	0.137
C20:3 omega 6, DGLA	1.70±0.14	1.29±0.09*	0.025
C20:4 omega 6, ARA	12.84±1.08	8.63±1.24*	0.021
C20:5 omega 3, EPA	0.62±0.04	0.32±0.04***	≤0.0001
C22:5 omega 3, DPA	1.45±0.11	0.96±0.09**	0.003
C22:6 omega 3, DHA	3.44±0.45	2.62±0.38	0.182
SFA	55.92±3.08	65.58±2.56*	0.028
MUFA	15.32±0.90	13.30±0.76	0.105
PUFA	28.75±2.37	21.11±1.94*	0.024
omega 6	23.25±1.84	17.22±1.54*	0.023
omega 3	5.50±0.54	3.90±0.46*	0.038
omega 6/ omega 3	4.32±0.15	4.68±0.44	0.45
SFA/MUFA	3.82±0.39	5.12±0.43*	0.04
Unsaturation index, UI	107.63±10.01	80.00±8.85	0.055
Peroxidation index,PI	97.39±9.56	70.00±9.03	0.053

Fatty acid values of the RBC membranes were also evaluated for their correlations with the percentage distributions of the 8 spectral end members expressed as mean ± s.e.m (standard error of the mean) and reported in the heatmaps of Fig. 4 of the main text, whereas Supplementary Table 4 reports the statistically significant values in controls and H_2O_2-treated RBC, respectively.

Supplementary Table 4. Correlations of HSI spectral distributions and fatty acid composition of RBC membranes. Correlations between the fatty acid composition of RBC membranes isolated from untreated and 1.5% H_2O_2-treated EDTA-containing whole blood samples (see Supplementary Table 3) and the HSI data from RBC images of the same samples (Fig. 1e).

Correlations HDFM spectra-FAME and indexes	Untreated RBC (n=9)		1.5% H_2O_2-treated RBC (n=9)	
	R+/-	significant p value	R+/-	significant p value
Spectrum 1-C16:0	+0.683	0.05		
Spectrum 1-11cis C18:1	-0.711	0.038	-0.717	0.037
Spectrum 1- C18:2 omega 6	/	/	-0.750	0.025
Spectrum 1-SFA/MUFA	+0.683	0.05	/	
Spectrum 4-C16:0	+0.767	0.021	/	/
Spectrum 4-C18:0	+0.683	0.05	+0.7	0.043
Spectrum 4-C18:2 omega 6	-0.750	0.025	-0.750	0.025
Spectrum 4-C20:4 omega 6	-0.867	0.005	/	/
Spectrum 4-C20:5 omega 3	/	/	-0.669	0.05
Spectrum 4-SFA	+0.783	0.017	/	/
Spectrum 4-MUFA	-0.683	0.05	/	/
Spectrum 4-PUFA	-0.750	0.025	/	/
Spectrum 4-omega 6	-0.750	0.025	/	/
Spectrum 4-SFA/MUFA	+0.683	0.05	/	/
Spectrum 4-UI	-0.683	0.05	/	/
Spectrum 4-PI	-0.750	0.025	/	
Spectrum 5-C18:0	/	/	0.833	0.008
Spectrum 5-C18:2 omega 6	/	/	-0.7	0.043
Spectrum 5-22:6 omega 3	/	/	-0.833	0.008
Spectrum 5-PUFA	/	/	-0.700	0.043
Spectrum 5-omega 3	/	/	-0.850	0.006
Spectrum 5-UI	/	/	-0.783	0.017
Spectrum 5-PI	/	/	-0.783	0.017
Spectrum 6-C18:0	/	/	+0.7	0.043
Spectrum 6-C18:2 omega 6	/	/	-0.8	0.014
Spectrum 7-C16:0	+0.7	0.043		
Spectrum 7-C20:4 omega 6	-0.733	0.031		
Spectrum 7-SFA	+0.733	0.031		
Spectrum 7-MUFA	-0.683	0.05		
Spectrum 7-omega 6/omega 3	/	/	+0.767	0.021
Spectrum 7-UI	-0.683	0.05	/	/
Spectrum 8-C16:0	-0.833	0.008	/	/
Spectrum 8-C18:0	-0.8	0.014	-0.717	0.037
Spectrum 8-18:2 omega 6	+0.8	0.014	+0.833	0.008
Spectrum 8-20:4 omega 6	-0.783	0.017	/	/
Spectrum 8-22:5 omega 3	/	/	+0.733	0.031
Spectrum 8-22:6 omega 3	/	/	+0.7	0.043
Spectrum 8-SFA	-0.817	0.011	/	/
Spectrum 8-MUFA	+0.7	0.043	/	/
Spectrum 8-PUFA	+0.8	0.014	/	/
Spectrum 8-omega 6	+0.8	0.014	/	/
Spectrum 8-omega 3	/	/	+0.7	0.043
Spectrum 8-SFA/MUFA	-0.783	0.017	/	/
Spectrum 8-UI	+0.8	0.014	/	/
Spectrum 8-PI	+0.8	0.014	/	/

Supplementary Table 5. Correlations of HSI spectral distributions and the values of the Na^+/K^+-ATPase activity in RBC membranes of neurotypical (NT) and Autism Spectrum Disorder (ASD) affected children. The statistically significant values are reported in the graphs of Figure 4 of the Main text. Statistical comparison was performed by applying non-parametric two-sided Mann-Whitney test (p=1.149E-34).

Correlations HDFM spectra- Na^+/K^-ATPase activity	NT (n=30)		AU(n=26)	
	slope	**p value**	**slope**	**p value**
Sp1- Na^+/K^-ATPase activity	0.0006	0.98	-0.026	0.61
Sp2- Na^+/K^-ATPaseactivity	-0.055	0.027	-0.06	0.092
Sp3- Na^+/K^-ATPase activity	-0.050	0.035	-0.15	0.0008
Sp4- Na^+/K^-ATPase activity	0.04	0.104	0.023	0.57
Sp5- Na^+/K^-ATPase activity	0.08	0.014	0.063	0.035
Sp6- Na^+/K^-ATPase activity	0.013	0.23	-0.009	0.83
Sp7- Na^+/K^-ATPase activity	0.058	0.06	0.0855	0.083
Sp8- Na^+/K^-ATPase activity	-0.017	0.28	-0.0009	0.96

3. Analysis of spectral data with Auto Contractive Map (Auto-CM)

The Auto-Contractive Map (Auto-CM) is a new paradigm of Artificial Neural Networks (ANNs). The Auto-CM differs from the traditional ANNs in a number of important aspects, mainly on the initialization of the weights and the conditions under which convergence is achieved.[16]

i. The mathematical representation of the AutoCM

Before we build the contractive map (CM), all the connections can be initialized either by equal values or by randomly selected values. The best practice is to initialize all the connections with the same positive value, close to zero.

The learning algorithm of CM may be summarized in four steps:

1. Signal Transfer from the Input into the Hidden layer;
2. Adaptation of the connections value between the Input layer and the Hidden layer; *
3. Signal Transfer from the Hidden layer into the Output layer; *
4. Adaptation of the connections value between the Hidden layer and the Output layer.

(*): step 2 and 3 may take place in parallel.

We define as $m^{[s]}$ the units of the Input layer (sensors), scaled between 0 and 1, as $m^{[h]}$ the units of the Hidden layer and as $m^{[t]}$ the units of the Output layer (system target). We define **v** the vector of monodedicated connections, **w** the matrix of the connections between Hidden layer and Output layer, and *n* the discrete time of the weights evolution. The signal forward transfer equations and learning are:

a. Signal transfer from the Input to the Hidden:

$$m_{i_{(n)}}^{[h]} = m_{i_{(n)}}^{[s]} \left(1 - \frac{v_{i_{(n)}}}{C} \right) \quad (1)$$

where C = Positive real number, named Contractive Factor.

b. Adaptation of the connections $v_{i_{(n)}}$ through the $\Delta v_{i_{(n)}}$ trapping the energy difference generated by the equation (1):

$$\Delta v_{i_{(n)}} = \left(m_{i_{(n)}}^{[s]} - m_{i_{(n)}}^{[h]} \right) \cdot \left(1 - \frac{v_{i_{(n)}}}{C} \right); \tag{2}$$

$$v_{i_{(n+1)}} = v_{i_{(n)}} + \Delta v_{i_{(n)}}; \tag{3}$$

c. Signal transfer from the Hidden to the Output:

$$Net_{i_{(n)}} = \sum_{j}^{N} m_{j_{(n)}}^{[h]} \cdot \left(1 - \frac{w_{i,j_{(n)}}}{C} \right); \tag{4}$$

$$m_{i_{(n)}}^{[t]} = m_{i_{(n)}}^{[h]} \left(1 - \frac{Net_{i_{(n)}}}{C} \right). \tag{5}$$

d. Adaptation of the connections $w_{i,j_{(n)}}$ through the $\Delta w_{i,j_{(n)}}$ trapping the energy differences generated by the equation (5):

$$\Delta w_{i,j_{(n)}} = \left(m_{i_{(n)}}^{[h]} - m_{i_{(n)}}^{[t]} \right) \cdot \left(1 - \frac{w_{i,j_{(n)}}}{C} \right) \cdot m_{j_{(n)}}^{[h]}; \tag{6}$$

$$w_{i,j_{(n+1)}} = w_{i,j_{(n)}} + \Delta w_{i,j_{(n)}} \tag{7}$$

The value $m_{j_{(n)}}^{[h]}$ of (6) is used to proportion the change of the connection $w_{i,j_{(n)}}$ to the energy liberated by the node $m_{j_{(n)}}^{[h]}$ in favour of node $m_{i_{(n)}}^{[t]}$.

The learning process, considered as the adjustment of the connections in relation to the minimization of Energy, corresponds to the continuous acceleration and deceleration of velocities of the signals inside the ANN connection matrix.

This can be mathematically described with the CM convergence equation:

$$\lim_{n \to \infty} v_{i_{(n)}} = C. \tag{8}$$

when $v_{i_{(n)}} = C$, then $\Delta v_{i_{(n)}} = 0$ (eq 2), and $m_{i_{(n)}}^{[h]} = 0$ (eq 1) and, consequently, $\Delta w_{i,j_{(n)}} = 0$ (eq 6).

We define four new variables that play a key role during the AutoCM learning process:

1. ε is the contractive factor of the first layer of AutoCM weights:

$$\varepsilon = 1 - \frac{v_{i_{(n)}}}{C}.$$

2. η is the contractive factor of the second layer of AutoCM weights:

$$\eta = 1 - \frac{w_{i,j_{(n)}}}{C}$$

3. φ is the contractive factor between the Hidden nodes and the Input nodes :

$$\varphi = m_{i_{(n)}}^{[s]} - m_{i_{(n)}}^{[h]};$$

4. λ is the contractive factor between the Output nodes and the Hidden nodes :

$$\lambda = m_{i_{(n)}}^{[h]} - m_{i_{(n)}}^{[t]}.$$

Then we demonstrate how $\Delta v_{i_{(n)}}$ changes during the CM learning phase.
Let us suppose that:

$$\frac{v_{i_{(n)}}}{C} = 1 - \varepsilon, \text{ where } \varepsilon \text{ is a small positive real number close to zero.};$$

Equation (2) can be rewritten as:

$$\Delta v_{i_{(n)}} = (m_{i_{(n)}}^{[s]} - m_{i_{(n)}}^{[s]} \cdot (1 - \frac{v_{i_{(n)}}}{C})) \cdot (1 - \frac{v_{i_{(n)}}}{C}) = m_{i_{(n)}}^{[s]} \cdot \frac{v_{i_{(n)}}}{C} \cdot (1 - \frac{v_{i_{(n)}}}{C}); \quad \text{(2a)}$$

Since $\frac{v_{i_{(n)}}}{C} = 1 - \varepsilon$, then :

$$\Delta v_{i_{(n)}} = m_{i_{(n)}}^{[s]} \cdot (1 - \varepsilon) \cdot (1 - (1 - \varepsilon)) = m_{i_{(n)}}^{[s]} \cdot (1 - \varepsilon) \cdot \varepsilon. \quad \text{(2b)}$$

Equation (2b) shows the parabolic dynamics of Δv_i.
Considering (2b) we can write:

$$\Delta v_{i_{(n)}} < \varepsilon. \quad \text{(2c)}$$

Equation (2c) means that the increment of $\Delta v_{i_{(n)}}$ will always be smaller than the quantity that $v_{i_{(n)}}$ needs to reach up to *C*.
At this point we can re-write the equation (3) as :

$$v_{i_{(n+1)}} = C \cdot (1 - \varepsilon)_{i_{(n)}} + m_{i_{(n)}}^{[s]} \cdot (1 - \varepsilon) \cdot \varepsilon. \quad \text{(3a)}$$

Consequently :

$$\lim_{\varepsilon \to 0} v_{i_{(n)}} = C \quad \text{(3b)}$$

Further, the contractive factor of the equations (1) and (5) suggests that:

$$m_{i_{(n)}}^{[t]} < m_{i_{(n)}}^{[h]} < m_{i_{(n)}}^{[s]}; \quad \text{(1-5)}$$

In fact :

$$m_{i_{(n)}}^{[h]} = m_{i_{(n)}}^{[s]} \cdot \varepsilon; \quad \text{(1a)}$$

and :

$$m_{i_{(n)}}^{[t]} = m_{i_{(n)}}^{[h]} \cdot \varepsilon \cdot (1 - Net_{i_{(n)}}). \quad \text{(5a)}$$

Now it is possible describe the relationship between $\Delta v_{i_{(n)}}$ and $\Delta w_{i,j_{(n)}}$.
From the equation (1-5) we can suppose that:

$$m_{i_{(n)}}^{[h]} = m_{i_{(n)}}^{[s]} - \varphi; \text{ where } \varphi \text{ is a small positive real number close to 0}; \quad \text{(1b)}$$

And

$$m_{i_{(n)}}^{[t]} = m_{i_{(n)}}^{[h]} - \lambda; \text{ where } \lambda \text{ is a small positive real number close to 0}; \quad \text{(5b)}$$

(5c) $$m_{i_{(n)}}^{[t]} = m_{i_{(n)}}^{[t]} - (\varphi + \lambda).$$

At this point equation (2) can be rewritten as:

(2d) $$\Delta v_{i_{(n)}} = (m_{i_{(n)}}^{[s]} - (m_{i_{(n)}}^{[s]} - \varphi)) \cdot (1 - \frac{v_{i_{(n)}}}{C}) = \varphi \cdot (1 - \frac{v_{i_{(n)}}}{C}) = \varphi \cdot \varepsilon.$$

In a similar way we can rewrite the equation (6) :

(6a) $$\Delta w_{i,j_{(n)}} = ((m_{i_{(n)}}^{[s]} - \varphi) - (m_{i_{(n)}}^{[s]} - (\varphi + \lambda)) \cdot (m_{i_{(n)}}^{[s]} - \varphi) \cdot (1 - w_{i,j_{(n)}}) = \lambda \cdot (m_{i_{(n)}}^{[s]} - \varphi) \cdot (1 - w_{i,j_{(n)}}).$$

Now we can rewrite $\frac{w_{i,j_{(n)}}}{C} = 1 - \eta$ (where η has to be a positive real number smaller than 1).

So :

(2e) $$\Delta v_{i_{(n)}} = \varphi \cdot \varepsilon;$$

And

(6b) $$\Delta w_{i,j_{(n)}} = \lambda \cdot (m_{i_{(n)}}^{[s]} - \varphi) \cdot \eta;$$

Considering the equation (5a) in this form:

(5b)
$$m_{i_{(n)}}^{[s]} \cdot \varepsilon \cdot Net_{i_{(n)}} = m_{i_{(n)}}^{[s]} \cdot \varepsilon - m_{i_{(n)}}^{[t]};$$
$$Net_{i_{(n)}} = \frac{m_{i_{(n)}}^{[s]} \cdot \varepsilon - m_{i_{(n)}}^{[t]}}{m_{i_{(n)}}^{[s]} \cdot \varepsilon} = \frac{m_{i_{(n)}}^{[s]} \cdot \varepsilon - (m_{i_{(n)}}^{[s]} \cdot \varepsilon - \lambda)}{m_{i_{(n)}}^{[s]} \cdot \varepsilon} = \frac{\lambda}{m_{i_{(n)}}^{[s]} \cdot \varepsilon}.$$

It is now possible to estimate the λ contractive factor between Hidden and Output units:

(5c) $$\lambda = m_{i_{(n)}}^{[s]} \cdot \varepsilon \cdot Net_{i_{(n)}}.$$

From (5c) we can write:

(5d) $$\lambda = m_{i_{(n)}}^{[s]} \cdot (1 - \frac{v_{i_{(n)}}}{C}) \cdot Net_{i_{(n)}}$$

and so:

(5e) $$\lim_{v_{i(n)} \to C} \lambda = 0$$.

We can substitute (5c) in (6b):

(6c) $$\Delta w_{i,j_{(n)}} = m_{i_{(n)}}^{[s]} \cdot \varepsilon \cdot Net_{i_{(n)}} \cdot (m_{i_{(n)}}^{[s]} - \varphi) \cdot \eta;$$

Since $m_{i_{(n)}}^{[s]} - \varphi = m_{i_{(n)}}^{[s]} \cdot \varepsilon$, then

(6d) $$\Delta w_{i,j_{(n)}} = (m_{i_{(n)}}^{[s]} \cdot \varepsilon)^2 \cdot Net_{i_{(n)}} \cdot \eta;$$

And

(6e) $$\lim_{\varepsilon \to 0} \Delta w_{i,j_{(n)}} = 0$$

Considering equation (7) :

(7a) $$w_{i,j_{(n+1)}} = C \cdot (1 - \eta)_{i,j_{(n)}} + (m_{i_{(n)}}^{[s]} \cdot \varepsilon)^2 \cdot Net_{i_{(n)}} \cdot \eta;$$

From (7a) we can conclude :

$$\lim_{\varepsilon \to 0} w_{i,j_{(n)}} = C - C \cdot \eta_{i,j_{(n)}}$$

(7b)

So this means that at the beginning of training the Input and Hidden units will be very similar (equation (1)), and, consequently, $\Delta v_{i_{(n)}}$ will be very small (equation (2e)), while for the same reason λ, initially will be large (equation (5c)) and $\Delta w_{i,j_{(n)}}$ larger than $\Delta v_{i_{(n)}}$ (equation (5c)).

During the training, while $v_{i_{(n)}}$ slowly increases, $m_{i_{(n)}}^{[h]}$ decreases, so φ increases and, consequently, $\Delta w_{i,j_{(n)}}$ continues to decrease monotonically (λ becomes smaller, see equation (5c)) and $\Delta v_{i_{(n)}}$ increases faster. When λ becomes close to zero, $m_{i_{(n)}}^{[h]}$ is only slightly larger that $m_{i_{(n)}}^{[t]}$ (see equation (5b)). At this point, $\Delta v_{i_{(n)}}$ is on the global maximum of the equation $(1-\varepsilon)\cdot\varepsilon$ (see (2b)) and after this critical point $\Delta v_{i_{(n)}}$ will decrease symmetrically toward zero.

ii. Auto CM: Theoretical consideration

Auto Contractive Maps do not behave as regular artificial neural networks (ANN):

a. Learning starts from all connections initialised with the same value. So they do not suffer the problem of the symmetric connections.
b. During training, they develop connections for only positive values. Therefore, Auto CM does not have inhibitory relations among nodes, but only different strengths of excitatory connections.
c. Auto CM can learn in hard conditions, that is, when the connections of the main diagonal of the second connection matrix are removed. When the learning process is organized in this way, Auto CM seems to find specific relationships between each variable and any other. Consequently, from an experimental point of view, it seems that the ranking of its connections matrix is equal to the ranking of the joint probability between each variable and the others.
d. After learning, any input vector, belonging to the training set, will generate a null output vector. So, the energy minimization of the training vectors is represented by a function through which the trained connections absorb the input training vectors completely. Auto CM seems to learn to transform itself in a dark body.
e. At the end of the training phase ($\Delta w_{i,j} = 0$), the components of the weights vector **v** reach the same value :

$$\lim_{n \to \infty} v_{i_{(n)}} = C \,.$$

(8)

The matrix **w**, then, represents the CM knowledge for the entire dataset.

It is possible to transform the **w** matrix in a probabilistic joint association between the variables *m***:**

$$p_{i,j} = \frac{w_{i,j}}{\sum_{j=1}^{N} w_{i,j}};$$

(9)

$$P(m_j^{[s]}) = \sum_{i}^{N} p_{i,j} = 1$$

(10)

The new matrix **p** can be considered as the probability of transition from any state-variable to any other:

$$P(m_i^{[t]} \middle| m_j^{[s]}) = p_{i,j} \,.$$

(11)

g. At the same time, the matrix **w** can be transformed into a non-Euclidean distance metric (u-metric), with the main diagonal of the **w** matrix fixed at value N.

If we consider N as a limit value for all the weights of the **w** matrix, we can write:

$$d_{i,j} = N - w_{i,j}$$

(12)

The new matrix **d** is also a squared symmetric matrix where the main diagonal represents the zero distance between each variable from itself.

iii. The Contractive Factor

Another way to interpret the squared weights matrix of the AutoCM system is to assume each variable of the dataset as a vector composed of all its values. Then, the dynamic value of each connection between two variables represents the local velocity of their mutual attraction caused by their mutual vectors similarity, with increasing similarity, increasing the attraction speed between the vectors. When two variables are attracted by each other, they contract proportionally to the original Euclidean space between them. The limit case is when two variables are identical, in this case the space contraction should be infinite and the two variables should collapse at the same point.
We can extract from each weight of a trained AutoCM this specific contractive factor

$$F_{i,j} = \left(1 - \frac{w_{i,j}}{C}\right)^{-1}; \quad 1 \le F_{i,j} \le \infty. \tag{9a}$$

This is interesting for the following reasons:

1. it is the inverse of the equation used as the contractive factor during the AutoCm training;
2. considering equation (3b) , each mono-connection v_i at the end of training will reach the value C. In this case the contractive factor will be infinite because the two variables connected by the weight are the same variable.
3. considering equation (7b), each weight $w_{i,j}$, at the end of training will always be smaller than C. This means that the contractive factor for each weight of the matrix that we consider will always be non-infinite. In fact, in the case of the weight $w_{i,i}$, when the variable is connected with itself, the variable has also received the influences of all other variables (the matrix $\mathbf{w}$ is a squared matrix where each variable is linked to the other). Consequently, this variable has not remained exactly the same.

At this point, we can calculate the contractive distance between each variable and any other, modifying the original Euclidean distance with a specific contractive factor.
The Euclidean distance among the variables in the dataset is given by the following equation:

$$d_{i,j}^{[Eucliden]} = \sqrt{\sum_{k}^{R} (x_{i,k} - x_{j,k})^2}; \tag{10a}$$

where :

$R =$ the number of the records of the assigned dataset;

$x_{i,k}$ and $x_{j,k} =$ the i-th value and the j-th value of two variables in the k-th record.

And, consequently, the AutoCM distance matrix among the same variables is:

$$d_{i,j}^{[AutoCM]} = \frac{d_{i,j}^{[Euclidean]}}{F_{i,j}}. \tag{11a}$$

Supplementary References

1. Barghava, A. *et al*. Hyperspectral imaging and its applications: a review. *Heliyon* 10, e33208 (2024).
2. Gallucci, M. *et al*. Serum folate, homocysteine, brain atrophy, and auto-CM system: The Treviso Dementia (TREDEM) study. *J. Alzheimers Dis.* 38, 581–587 (2014).

3. Gao, P. F., Lei, G. & Huang, C. Z. Dark-field microscopy: recent advances in accurate analysis and emerging applications. *Anal. Chem.* 93, 4707–4726 (2021).
4. La Spina, R. *et al*. Dark field microscopy-based biosensors for the detection of E. coli in Environmental Water Samples. *Sensors* 19, 4652 (2019).
5. Tanaka, K., Fujioka, Y., Kubono, A. & Akiyama, R. Electrically developed morphology of carbon nanoparticles in suspensions monitored by in situ optical observations under sinusoidal electric field. *Colloid Polym. Sci.* 284, 562–567 (2006).
6. Ishmukhametov, I. & Fakhrullin, R. Dark-field hyperspectral microscopy for carbon nanotubes bioimaging. *Appl. Sci.* 11, 12132 (2021).
7. Lawrence, S. Enhanced darkfield optical microscopy opens new nano-scale imaging possibilities. *Microsc. Today* 29, 50–55 (2021).
8. Wang, H., Zhang, T. & Zhou, X. Dark-field spectroscopy: development, applications and perspectives in single nanoparticle catalysis. *J Phys. Condens. Matter* 31, 473001 (2019).
9. Gorbachevskii, M. V. *et al*. Fluorescent gold nanoclusters stabilized on halloysite nanotubes: in vitro study on cytotoxicity. *Appl. Clay Sci.* 207, 106106 (2021).
10. Austin, C. A. *et al*. Distribution and accumulation of 10 nm silver nanoparticles in maternal tissues and visceral yolk sac of pregnant mice, and a potential effect on embryo growth. *Nanotoxicology* 10, 654–661 (2016).
11. Fakhrullin, R., Nigamatzyanova, L. & Fakhrullina, G. Dark-field/hyperspectral microscopy for detecting nanoscale particles in environmental nanotoxicology research. *Sci. Total Environ.* 772, 145478 (2021).
12. Vasefi, F., MacKinnon, N. & Farkas, D. L. Chapter 16 - Hyperspectral and Multispectral Imaging in Dermatology. in Imaging in Dermatology (eds. Hamblin, M. R., Avci, P. & Gupta, G. K.) 187–201 (Academic Press, Boston, 2016). doi:10.1016/B978-0-12-802838-4.00016-9.
13. Conti, M. *et al*. Building up spectral libraries for mapping erythrocytes by hyperspectral dark field microscopy. *Biomed. Spectrosc. Imag.* 5, 175–184 (2016).
14. Giacometti, G. *et al*. High predictive values of RBC membrane-based diagnostics by biophotonics in an integrated approach for Autism Spectrum Disorders. *Sci. Rep.* 7, 9854 (2017).
15. Remigante, A. *et al*. Antioxidant activity of Quercetin in a H_2O_2-induced oxidative stress model in red blood cells: functional role of band 3 protein. *Int. J. Mol. Sci*. 23, 10991 (2022).
16. Buscema, M., Grossi, E., Snowdon, D. & Antuono, P. Auto-Contractive Maps: an artificial adaptive system for data mining. An application to Alzheimer disease. *Curr. Alzheimer Res.* **5**, 481–498 (2008).